PCCP

PAPER

View Article Online
View Journal | View Issue

Open Access Article. Published on 22 April 2025. Downloaded on 12/6/2025 4:39:31 PM.
This article is licensed under a Creative Commons Attribution 3.0 Unported Licence.

Check for updates

Cite this: *Phys. Chem. Chem. Phys.*, 2025, **27**, 9884

Hydrogen migration reactions *via* low internal energy pathways in aminobenzoic acid dications†

Onni Veteläinen,*[a] Morsal Babayan,[a] Lassi Pihlava,[b] Abdul Rahman Abid,[a] Antti Kivimäki,[c] Edwin Kukk,[b] Noelle Walsh,[c] Samuli Urpelainen,[a] Olle Björneholm,[d] Marko Huttula,[a] Matti Alatalo,[a] Minna Patanen[a] and Sergio Díaz-Tendero*[efg]

Received 31st January 2025,
Accepted 18th April 2025

DOI: 10.1039/d5cp00415b

rsc.li/pccp

Hydrogen migration is a ubiquitous phenomenon upon dissociation of organic molecules. Here we investigate the formation of a H_3O^+ fragment after core-level photoionization and Auger decay in aminobenzoic acid molecules – a process that requires the migration of at least two hydrogen atoms. Using photoelectron–photoion coincidence spectroscopy, the formation of a H_3O^+ fragment is observed to be more probable in *ortho*-aminobenzoic acid than in *meta*- and *para*-aminobenzoic acid. Energy-resolved Auger electron–photoion coincidences are measured for the *ortho*-isomer to investigate the internal energy dependence of the fragmentation channels, most notably of those producing H_3O^+. The corresponding fragmentation channels and their mechanisms are investigated by exploring the potential energy surface with *ab initio* quantum chemistry methods and molecular dynamics simulations. Excited-state modeling of dicationic *ortho*-aminobenzoic acid is used to interpret features in the Auger spectra and identify the electronic states contributing to the signals in the Auger electron photoion coincidence map. We show that populating low-energy excited states of the dication is sufficient to trigger hydrogen migration and produce H_3O^+ efficiently.

Introduction

Aminobenzoic acid (ABA) is an aromatic molecule with carboxyl (–COOH) and amino (–NH_2) functional groups. It has three isomers, *ortho*-, *meta*-, and *para*-ABA (*o*ABA, *m*ABA, and *p*ABA) depending on the positioning of the functional groups. In addition, *o*ABA and *m*ABA have two rotational conformers based on the rotation of the carboxyl group (we refer to the lowest energy rotamers as *o*ABA1 and *m*ABA1, see ESI† for more discussion on the rotational configurations). The richness of isomers and the importance of the involved functional groups in various biochemical reactions and syntheses make ABAs an interesting set of molecules to study the structural dependency of radiation-induced intramolecular reactions.[1–3]

Our previous photoelectron–photoion coincidence (PEPICO) study of *o*ABA and *m*ABA found that the fragmentation channels following core ionization and Auger decay are sensitive to the positioning of the functional groups, notably H_3O^+ and H_2O production rates are higher in the *ortho*-isomer.[4] The molecular geometry of aminobenzoic acid requires at least two hydrogen migration processes to form the H_3O^+ fragment. Hydrogen migration is a ubiquitous process in various chemical reactions and fragmentation processes following radiation damage.[5–8] The isomer dependency of H_3O^+ production in ABAs offers an excellent case study to understand such processes better. Being the protonated form of water, H_3O^+ itself is a common molecular ion in the universe, playing an important role in both terrestrial systems and atmospheric processes, objects in the solar system and even in interstellar media.[9–16] H_3O^+ is often formed from water and organic molecules and clusters following photoionization, for example by cosmic rays in the upper atmosphere. Signs of complex organic molecules, including amino acids and their precursors, have recently been reported to be found in asteroids[17,18] and meteorites,[19] and their formation and degradation in interstellar medium, like in ice grains, have gained a lot of interest.[20–22]

The formation mechanisms of H_3O^+ have been studied using various experimental techniques such as time-of-flight (TOF)

[a] Nano and Molecular Systems Research Unit, Faculty of Science, P.O. Box 3000, 90014 University of Oulu, Finland. E-mail: onni.vetelainen@oulu.fi
[b] Department of Physics and Astronomy, 20014 University of Turku, Finland
[c] MAX IV Laboratory, Lund University, 22100 Lund, Sweden
[d] Department of Physics and Astronomy, Uppsala University, Box 516, 751 20 Uppsala, Sweden
[e] Departamento de Química, Módulo 13, Universidad Autónoma de Madrid, 28049 Madrid, Spain. E-mail: sergio.diaztendero@uam.es
[f] Condensed Matter Physics Center (IFIMAC), Universidad Autónoma de Madrid, 28049 Madrid, Spain
[g] Institute for Advanced Research in Chemical Sciences (IAdChem), Universidad Autónoma de Madrid, 28049 Madrid, Spain

† Electronic supplementary information (ESI) available: Extended experimental details, molecular dynamics simulations, Auger profiles for selected fragments, partial charge analysis and microcanonical rate coefficients. See DOI: https://doi.org/10.1039/d5cp00415b

 This journal is © the Owner Societies 2025

Open Access Article. Published on 22 April 2025. Downloaded on 12/6/2025 4:39:31 PM. This article is licensed under a Creative Commons Attribution 3.0 Unported Licence.

mass spectroscopy as well as *ab initio* computational methods.[5,23–30] For example, in a pump–probe study of gas phase ethanol, Kling *et al.*[5] observed H_3O^+ formation from dicationic ethanol. Based on molecular dynamics simulations they proposed a double hydrogen migration mechanism, with the second hydrogen migration causing the C–O bond cleavage and H_3O^+ release within a timescale of several hundred femtoseconds. Shirota *et al.*[23] also presented a double hydrogen mechanism for the formation of H_3O^+ from the $C_2H_5O^+$ ion (a metastable intermediate in the photodissociation reactions of alcohols and ethers) based on *ab initio* calculations. Similar results for ethanol and $C_2H_5O^+$ were obtained with density functional theory calculations by Ma *et al.*,[26] who observed H_3O^+ formation in ethanol after electron beam irradiation. Hydrogen migration was also observed in ionized molecules of biological relevance, such as amino acids,[6,31,32] nucleosides,[33] sugar molecules,[34] and clusters of amino acids.[35]

Our previous study established a difference in the H_3O^+ formation between *o*ABA and *m*ABA. In this study, we confirm the isomer dependency of H_3O^+ production for all the ABA isomers by measuring the PEPICO spectra following carbon 1s ionization and subsequent fragmentation of dicationic *o*ABA and *p*ABA in the gas phase. Furthermore, to investigate the fragmentation dynamics of *o*ABA in more detail we measure the energy-resolved Auger electron photoion coincidence (AEPICO) spectra. The highest possible Auger electron energy is reached when the energy difference between the initial and final states of the Auger process is maximal, that is when the final state is the dicationic ground state. When the final state is an excited state of the dication, the Auger electron energy is necessarily lower. Therefore, higher Auger electron energies imply lower energy final states for the Auger process and thus lower internal energies available for the fragmentation processes. The energy-resolved AEPICO spectrum thus shows us the internal energies required for specific fragmentation processes, based on the Auger electron energy at which the cation signals appear. Similar internal energy – Auger electron energy mapping has been utilised *e.g.* in a study of dissociation timescales of the diiodothiophene dication.[36] We observe that the H_3O^+ signal appears in a narrow energy range right after the stable dication signal in the AEPICO map, *i.e.* the fragmentation process occurs with low internal energies of the dication and the corresponding Auger final state is some low-lying excited state of the dication. By modeling the excited states with *ab initio* quantum chemistry methods we can identify the final dicationic electronic states contributing to the H_3O^+ and other signals. We then explore the potential energy surface to identify multiple potential pathways of H_3O^+ formation, with activation energies that match the experiment. *Ab initio* molecular dynamics were also used to simulate the fragmentation processes.

Methods

Experimental details

The experiments were performed at the gas-phase endstation[37] of the FinEstBeAMS beamline[38,39] at the MAX IV Laboratory in Lund, Sweden. Powder-form samples of aminobenzoic acid ($C_7H_7NO_2$, molar mass 137.136 g mol^{-1}) were placed in a resistively heated oven in a glass crucible. Both studied isomers, *ortho*- and *para*-aminobenzoic acid (Sigma-Aldrich, Merck Group, St. Louis, US) had higher than 98% purity and were used without any further purification. Effusive beams of gas-phase molecules were created by heating the samples to ~50–60 °C (*o*ABA) and ~100 °C (*p*ABA). Non-coincidence Auger electron spectra were measured with a Scienta R4000 (Scienta Omicron GmbH) electron energy analyser. The photon energy of 350 eV was selected with an SX-700 type plane-grating monochromator (FMB Feinwerk-und Messtechnik GmbH, Berlin, Germany) with a 600-lines-mm^{-1} grating. The electron energy analyser was operated with a 50 eV pass energy and 0.8 mm curved entrance slit, yielding 100 meV kinetic energy resolution which is close to the lifetime broadening of C 1s core hole states in carbon compounds.[40] The spectrum was energy calibrated using the C 1s $\rightarrow$ $3\sigma^{-2}\ {}^1\Sigma_g$ Auger transition in CO_2 at 251.9 ± 0.1 eV[41] as a reference. The polarization vector of linearly polarized synchrotron radiation was parallel to the electron detection axis of the electron energy analyser, but to the first approximation, the Auger intensities should not depend on the photoionization anisotropy parameter β. However, since the β value of the atomic C 1s orbital is 2 (and only slightly lower in a molecular environment), this configuration typically maximises the photoelectron counts when recording C 1s PEPICO spectra. This is important for higher purity of PEPICO data as the electron analyser has a much smaller acceptance angle than the ion analyser.

The Scienta R4000 analyser is equipped with a fast position-sensitive detector (Quantar Inc., Model 3395A) to allow electron–ion coincidence measurements. The coincidence data was collected during two different experimental campaigns, and both times, the C 1s PEPICO spectrum of *o*ABA was collected to confirm reproducibility. In coincidence measurements, performed also with 350 eV photon energy, the electron analyser was operated in a constant kinetic energy mode with a pass energy of 200 eV. When an electron within the kinetic energy range of interest arrived at the detector, an electric field was ramped up to extract positive ions present in the interaction region towards a modified Wiley–McLaren type multi-hit-capable ion time-of-flight (TOF) spectrometer, which is equipped with a position-sensitive delay line detector (HEX80, RoentDek Handels GmbH). Details regarding the TOF settings can be found in the ESI.† A pulse generator operating at approximately 60 Hz was also used to trigger the ion extraction field. Since these pulses are not correlated with electron triggers, they lead only to "false" ion collection. These can then be used to subtract the false coincidence ion background from the electron-triggered data.[37,42] The amount of false coincidences was kept low by limiting the electron count rate to 10–20 counts s^{-1} by closing the exit slit of the monochromator to 25 μm. The data analysis was carried out using Igor Pro software (Wavemetrics, Inc. USA), augmented with curve fitting[43,44] and coincidence data handling macro packages by E. Kukk.

Computational details

Two computational approaches were used to study the fragmentation: by calculating potential energy landscapes of the

Open Access Article. Published on 22 April 2025. Downloaded on 12/6/2025 4:39:31 PM.
This article is licensed under a Creative Commons Attribution 3.0 Unported Licence.

dication (carried out only for *o*ABA1) and using molecular dynamics (for all isomers). The ground state potential energy surface exploration, including geometry optimizations for minima and transition states, intrinsic reaction coordinate calculations, frequency calculations and zero-point corrections, was performed using second-order Møller–Plesset perturbation theory[45] with the correlation consistent valence double-zeta basis set cc-pVDZ.[46] The singlet and triplet excited state energies of dicationic *o*ABA1 were calculated using the equation of motion coupled cluster method with single and double excitations (EOM-CCSD)[47,48] with the cc-pVTZ basis set, using the MP2/cc-pVDZ optimized geometry of the neutral molecule. The molecular dynamics were performed using the atom centered density matrix propagation model (ADMP).[49–51] ADMP belongs to the extended Lagrangian family of molecular dynamics methods, in which the electronic degrees of freedom are propagated by introducing a fictitious term in the Lagrangian. Here, all isomers of ABA (including the rotamers) were considered. Applying the Franck–Condon approximation, the dynamics of the dicationic systems were propagated starting from the optimized coordinates of the neutral molecules. Both the geometry optimizations and the molecular dynamics were done at the B3LYP[52,53]/6-31G(d,p)[54] level of density functional theory. At the beginning of each trajectory, the internal energy was assumed to be randomly distributed along the nuclear degrees of freedom in the dicationic ground state. Three internal energy estimates were used: 10 eV, 20 eV and 30 eV. For each molecule and internal energy estimate 1024 trajectories were computed. The propagation time for each trajectory was 250 fs, with a time step of 0.1 fs. All calculations were performed using the Gaussian16[55] computational chemistry package.

Results and discussion

Fig. 1 shows a schematic of the processes studied in *o*ABA and the structural formula of its lower energy rotational conformer *o*ABA1. Fig. 1(a) indicates the involved energy levels. The *o*ABA molecule in its neutral ground state in the gas-phase is core-ionised from the C 1s level using 350 eV photons. The core-ionised states are well separated in energy, and their identification and binding energies were determined using the results of our previous study.[4] The core-ionised states decay *via* Auger electron emission to double-ionised states. Due to a short core-hole lifetime (fs timescale) we can assume that dicationic excited states of the canonical structure of the neutral molecule are populated. The lowest DIP can be reached after a significant rearrangement in the dicationic final state, with a redistribution of the internal energy, as will be discussed later. The Auger spectrum (Fig. 1(b)) is a typical C 1s Auger electron spectrum of a multiatomic organic compound, a rather featureless broad asymmetric distribution of electrons from ∼280 eV to ∼215 eV. Compared to the overall broadness of the spectrum, we have used a very small step size of 50 meV to record the spectrum in order to resolve two small peaks, marked with an asterisk, at 267.9 and 269.1 eV at the high-energy onset of the spectrum. Fig. 1(c) shows four TOF spectra of coincident ions (false coincidence subtracted) related to C 1s photoelectrons

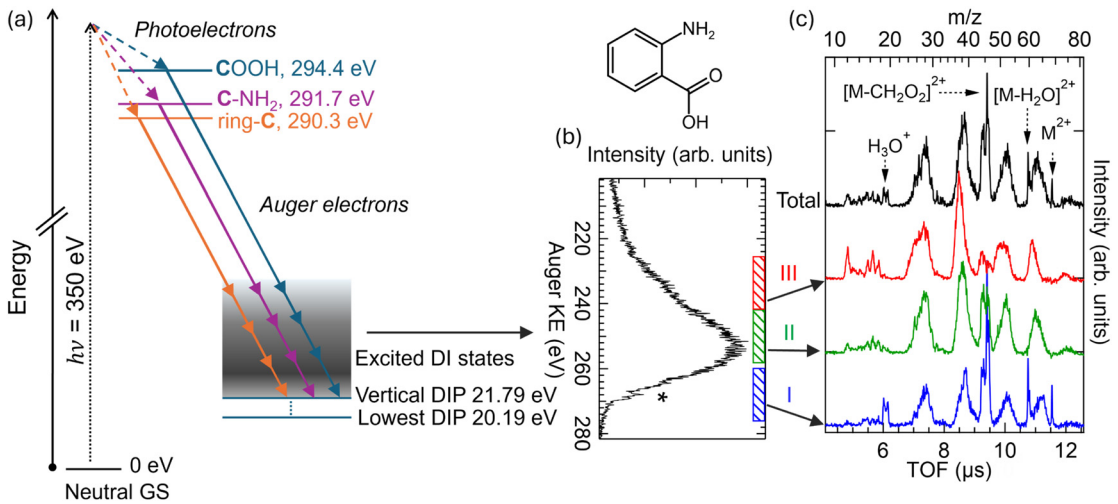

Fig. 1 A schematic of the processes and energy levels involved in this study with corresponding electron and ion spectra. (a) Energy level diagram (not to scale). The neutral ground state (GS) is set as the 0 of the energy scale. 350 eV photons initiate the process by photoionising the molecule from the C 1s levels. The binding energies (BEs) of chemically distinct carbon atoms are indicated next to the energy levels and taken from ref. 4. Core-ionised states decay *via* Auger decay to double-ionised (DI) states. The electronic transitions take place in the fs time scale, and thus the vertical double ionization potential (DIP) (calculated value) defines the onset of the experimental Auger electron spectrum. The state of the lowest DIP (calculated value) requires a significant restructuring of the molecule and is reached long after the Auger decay. (b) Molecular structure and the C 1s Auger electron spectrum of *o*ABA. The asterisk marks two peaks which are discussed in the text. The kinetic energy regions I–III are depicted with blue, green, and red, respectively, to the right part of the graph. (c) TOF spectra in coincidence with all C 1s photoelectrons (labelled as total, black line) and three Auger regions: high kinetic energy region I (blue), medium kinetic energy region II (green), and low kinetic energy region III (red). Stable dications and H_3O^+ are indicated in the spectrum. The structural formula of *o*ABA1 is shown.

Open Access Article. Published on 22 April 2025. Downloaded on 12/6/2025 4:39:31 PM.
This article is licensed under a Creative Commons Attribution 3.0 Unported Licence.

(black trace) and Auger electrons with low, medium, and high kinetic energies (red, green, and blue traces, respectively). Note that there is a double peak around m/z = 19 in the blue spectrum. This is a signature of the high kinetic energy of the detected ions where we lose those which are emitted perpendicular to the spectrometer axis.

Fig. 2 compares the TOF mass spectra of all three isomers recorded in coincidence with C 1s photoelectrons ($h\nu$ = 350 eV). The m/z ranges for the main detected ions are marked in Fig. 2, and the sharp peaks originating from doubly charged species with very low or no kinetic energy are indicated. The low m/z range contains CH_i^+ (i = 0,...,4), NH_j^+ (j = 0,...,4), and OH_k^+ (k = 0,...,3) fragments, followed by a broad region with ions for example $C_2H_n^+$, CNH_n^+, and COH_n^+ (n = 0,...,2, m/z ~ 26–30). The m/z range covering 37–41 is a typical range for benzene ring fragments which can here also include an amino group. $COOH^+$ has m/z of 45, and this signature is overlapped with two sharp peaks at ~44.6 and ~45.6, originating from doubly charged

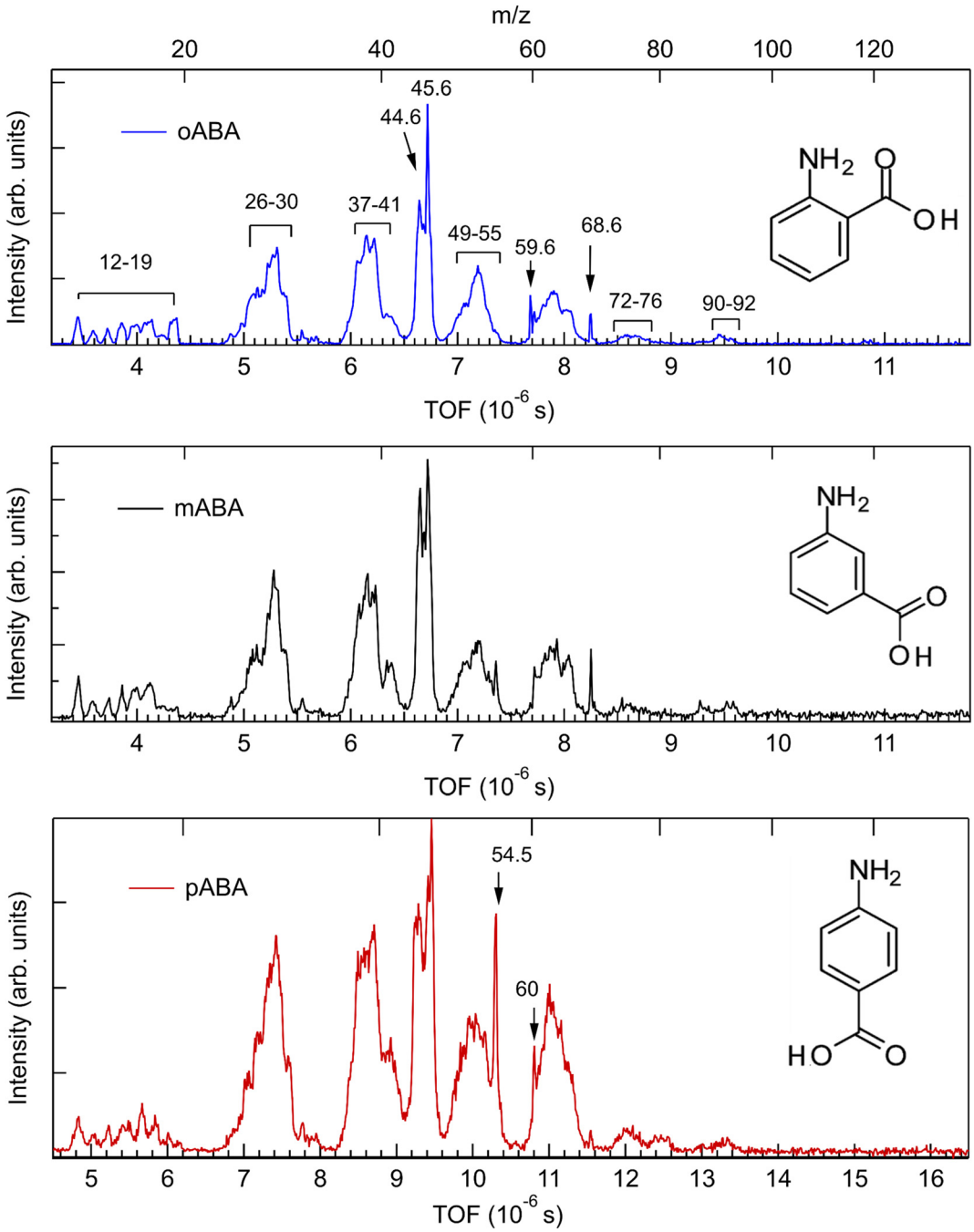

Fig. 2 TOF spectra of all aminobenzoic acid isomers, measured in coincidence with C 1s photoelectrons. The data in the spectra of *o*ABA and *m*ABA are taken from ref. 4, and they have been measured with a higher extraction field in the TOF spectrometer, and thus the TOF axis differs compared to *p*ABA. The m/z ratio is depicted as an indicative axis on the top.

Open Access Article. Published on 22 April 2025. Downloaded on 12/6/2025 4:39:31 PM.
This article is licensed under a Creative Commons Attribution 3.0 Unported Licence.

ions with masses of 89 and 91 amu, respectively. These doubly charged ions can be, for example, a parent ion which has lost a COOH-group and some additional hydrogens. The following m/z range 49–55 is again a typical range for benzene ring fragments, and the next doubly charged ion, especially strong for *p*ABA, is at m/z = 54.5. This is interpreted as a parent ion which has lost 28 amu, which indicates the emission of a CO or CNH_2 fragment. In *o*ABA, there is a sharp peak at m/z = 59.6, which would be a doubly charged parent which has lost a neutral fragment with a mass of 18 amu, the plausible interpretation being emission of neutral H_2O. Interestingly, in *m*ABA and *p*ABA a sharp peak is observed at m/z = 60, which would correspond to a fragment arising from the fragmentation of a doubly charged parent with a loss of 17 amu, *i.e.* neutral OH or NH_3. After m/z = 60, there is a region of ring fragments up to a doubly charged parent ion signature at m/z = 68.6, especially visible for *o*ABA and *m*ABA, but very small in *p*ABA. In all isomers, ring fragments around m/z = 74 are visible, as well as some signatures of $[M–COOH]^+$ and additional H-loss ions at m/z = 90–92. Notice that in Fig. 2 the m/z peaks 16, 17, and 19 have flat tops in the TOF spectra recorded for *o*ABA and *m*ABA, while in *p*ABA, the lower field setting resulted in the loss of some ions emitted perpendicular to the spectrometer axis, leading to double peak structures.

Fig. 3 shows the energy-resolved AEPICO coincidence map in the high energy region of the Auger electron, corresponding to KE region I in Fig. 1. The AEPICO map is constructed by presenting the Auger electron – ion events as a contour plot where the colour scale of the map refers to the number of coincidence events. The kinetic energy of the events Auger electron defines the position on the x-axis, while the TOF of the detected ion defines the placement with respect to the y-axis. The most important fragments discussed here are labelled in the projected TOF spectrum on the right-hand panel of the coincidence map. Some selected profiles are shown in the ESI† (see Fig. S1). The first, well-isolated intense signal from the right at 269.1 eV is due to the stable dication, and it matches the first peak labelled with an asterisk in Fig. 1(b). The H_3O^+ and $[M–H_3O]^+$ signals appear at 1.2 eV lower Auger kinetic energy than the stable dication, and these signals form the second peak marked with an asterisk in Fig. 1(b). They peak in a very narrow energy range, but H_3O^+ is produced in small amounts at lower Auger kinetic energies as well. Due to broadness of the lower field TOF peaks, there might also be a small contribution from the H_2O^+ fragment in the H_3O^+ signal. However, other channels such as $[M–H_2O]^{2+}$ and $[C_6H_5N]^{2+}$ dominate the fragmentation dynamics below 267 eV Auger kinetic energies (higher internal energies).

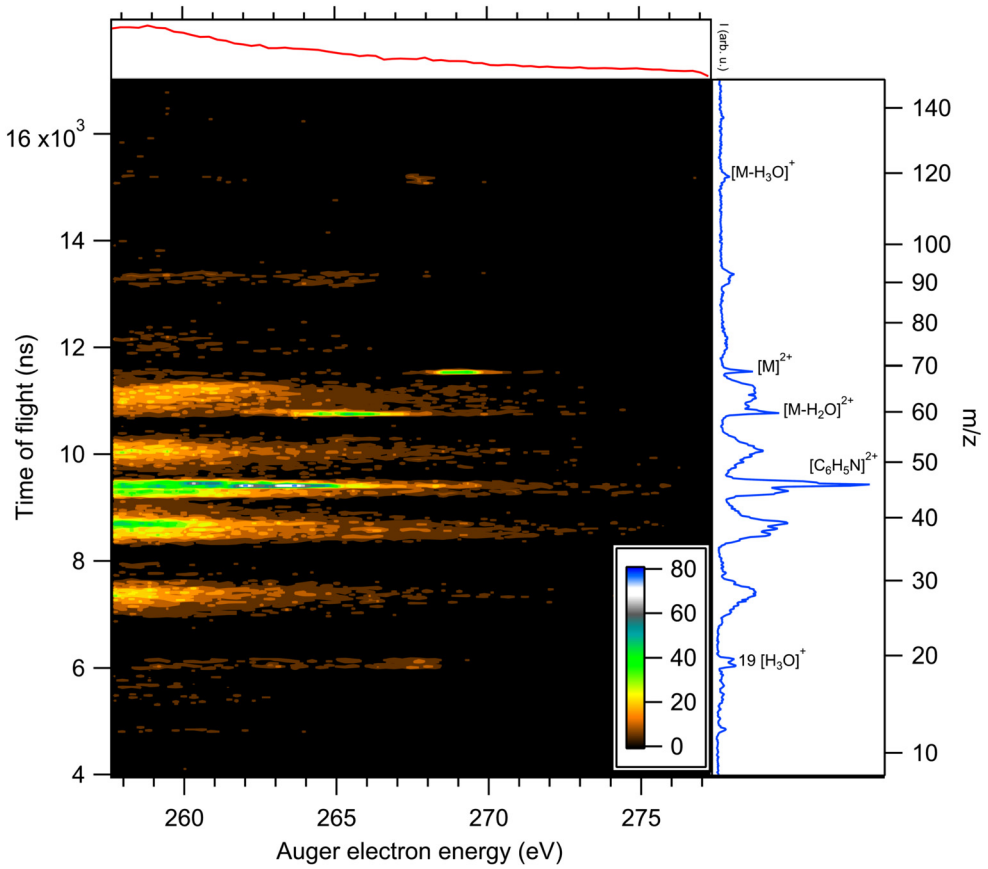

Fig. 3 Auger electron photoion coincidence map in the high Auger electron energy region (region I in Fig. 1). The color scale refers to the number of counts. The corresponding total Auger electron and TOF spectra are depicted in the top and right-hand panels respectively.

Open Access Article. Published on 22 April 2025. Downloaded on 12/6/2025 4:39:31 PM.
This article is licensed under a Creative Commons Attribution 3.0 Unported Licence.

Note that production of H_3O^+ in *o*ABA is mainly observed in the high-kinetic-energy region of the Auger electron spectrum, which corresponds to a low internal excitation energy in the remaining dication. We have obtained deeper insight into the double ionization in this region, and the subsequent fragmentation mechanisms with quantum chemistry calculations. We focus on the rotamer 1 of *o*ABA, which is expected to be the dominant configuration at the experimental temperature, based on the energy difference between the *ortho*-rotamers ($\sim$120 meV).[4] First, the high-kinetic-energy region of the Auger electron spectrum (see region I in Fig. 1(c) and 3) was investigated by excited states calculations of dicationic *o*ABA using the geometry of the neutral molecule, computed at the MP2/cc-pVDZ level, *i.e.*, assuming vertical ionization in the Franck–Condon region. The excited states were modelled using the equation of motion coupled cluster method with single and double excitations (EOM-CCSD).[47,48] The results are presented in Table 1, and the energies are referred to the dicationic ground state. The vertical double ionization potential is the lowest possible energy final state in the Auger process assuming that nuclei do not have time to move in the core-ionised state (lifetime in order of a few fs), and thus corresponds to the highest possible Auger electron energy in the Auger electron spectrum. Lower Auger electron energies correspond to excited states as the Auger final states. We concentrate on the low-lying excited states as in that region the most interesting spectral features are observed, namely the peak at 269.1 eV due to stable dications and 267.9 eV where H_3O^+ production occurs. Using the results in Table 1 we may interpret the AEPICO map features in Fig. 3. A single Gaussian fit to the first signal from the right (*i.e.* the stable dication M^{2+} signal) in the AEPICO map depicted in Fig. 3 gives a full-width-at-half-maximum (FWHM) of 1.4 eV, which is considerably higher than the experimental broadening of 0.45 eV. This can be due to significant vibrational broadening, and/or two or more overlapping electronic states. A double Gaussian fit also gives a total FWHM of 1.4 eV and a peak separation of 0.65 eV, which matches well the computed first triplet excitation energy of 0.59 eV. We can conclude that both the dicationic ground state S_0 and the first triplet state T_1 can contribute to the M^{2+} signal. Fitting the H_3O^+ signal was much more challenging due to the low counts, but it is approximately as wide as the M^{2+} signal, and therefore likely composed of multiple electronic states as well. We propose that these are the T_2, S_1, S_2 and T_3 excited states which are grouped closely together in energy and whose average energy (1.56 eV) is 1.26 eV higher than the average energy of the S_0 and T_1 states, matching the experimental peak separation of 1.2 eV between the M^{2+} and H_3O^+ signals. The higher energy S_3, S_4 and T_4 excited states then contribute to signals further to the left in the coincidence map, where multiple fragmentation channels such as the $[M–H_2O]^{2+}$ and $C_6H_5N^{2+}$ channels start to overlap.

Table 1 The energies of low-lying *o*ABA dicationic excited states at the EOM-CCSD/cc-pVTZ level and MP2/cc-pVDZ optimized geometry. S and T indicate singlet and triplet states, respectively. Energies are relative to the dicationic ground state S_0 energy, and calculated at the neutral ground state geometry

Singlet states	S_1	S_2	S_3	S_4
Energy (eV)	1.45	1.51	2.51	3.92
Triplet states	T_1	T_2	T_3	T_4
Energy (eV)	0.59	1.39	1.88	2.33

The fragmentation mechanisms of dicationic ABA were investigated through an exploration of the potential energy surface (PES) as well as *ab initio* molecular dynamics simulations. Fig. 4 presents the results of the PES exploration. We assume a very efficient energy redistribution from the electronic excited states populated in the Auger process, towards nuclear degrees of freedom in electronic ground state (electron–phonon coupling). Thus, the PES exploration is carried out in the electronic ground state. The minimum Min 1 (highlighted in red) is reached by relaxation following vertical ionization. Hydrogen migration (through transition state TS 1, highlighted in green) followed by H_2O roaming connect Min 1 to a more stable configuration in the minimum Min 2 (highlighted in blue). The reconfiguration to this more stable structure is a common step in the calculated pathways.

Fig. 4(a) shows a straightforward water roaming pathway starting from Min 2 with subsequent H_3O^+ release. The proton abstraction causes the initial benzene ring to be transformed into a five-membered ring with a cyclopentadiene configuration. The emission of neutral water is also depicted here and the energy required for the barrierless release of H_2O lies 1.73 eV above the vertical double ionisation potential (VIP in Fig. 4). Apart from the water emission, the highest energy point in this pathway corresponds to the transition state TS 1, so H_3O^+ release becomes accessible with an internal energy of 1.05 eV. A more complicated series of hydrogen and water migrations is depicted in Fig. 4(b), but the endpoint is the same five-atom-ring structure as in Fig. 4(a). The highest energy point in this figure is 23.73 eV, so the pathway is accessible with a slightly higher internal energy of 1.96 eV, which is also higher than the H_2O emission energy of 1.73 eV. Finally, Fig. 4(c) depicts water roaming pathways starting from Min 2 and the initial water-producing transition states towards the NH_2 group, from which either proton may be abstracted by the roaming water to produce H_3O^+. The highest energy point here is again the first transition state TS 1, so the pathways given in this panel are also accessible with an internal energy of 1.05 eV, which is in rather good agreement with the experimental peak separation between the stable dication and H_3O^+ signals (see Fig. 3). A comparison of the microcanonical coefficient rates of the pathways in Fig. 4 indicates that proton abstraction from the $–NH_2$ group is the most efficient process (see ESI† for more details). A partial charge analysis was also performed to investigate the flow of charge during the fragmentation pathways. The results can be found in the ESI.†

Among the aminobenzoic acid isomers, *o*ABA (specifically the rotamer 1) is the most stable in terms of total energy in the ground state. It has been suggested that the reason for its

Open Access Article. Published on 22 April 2025. Downloaded on 12/6/2025 4:39:31 PM.
This article is licensed under a Creative Commons Attribution 3.0 Unported Licence.

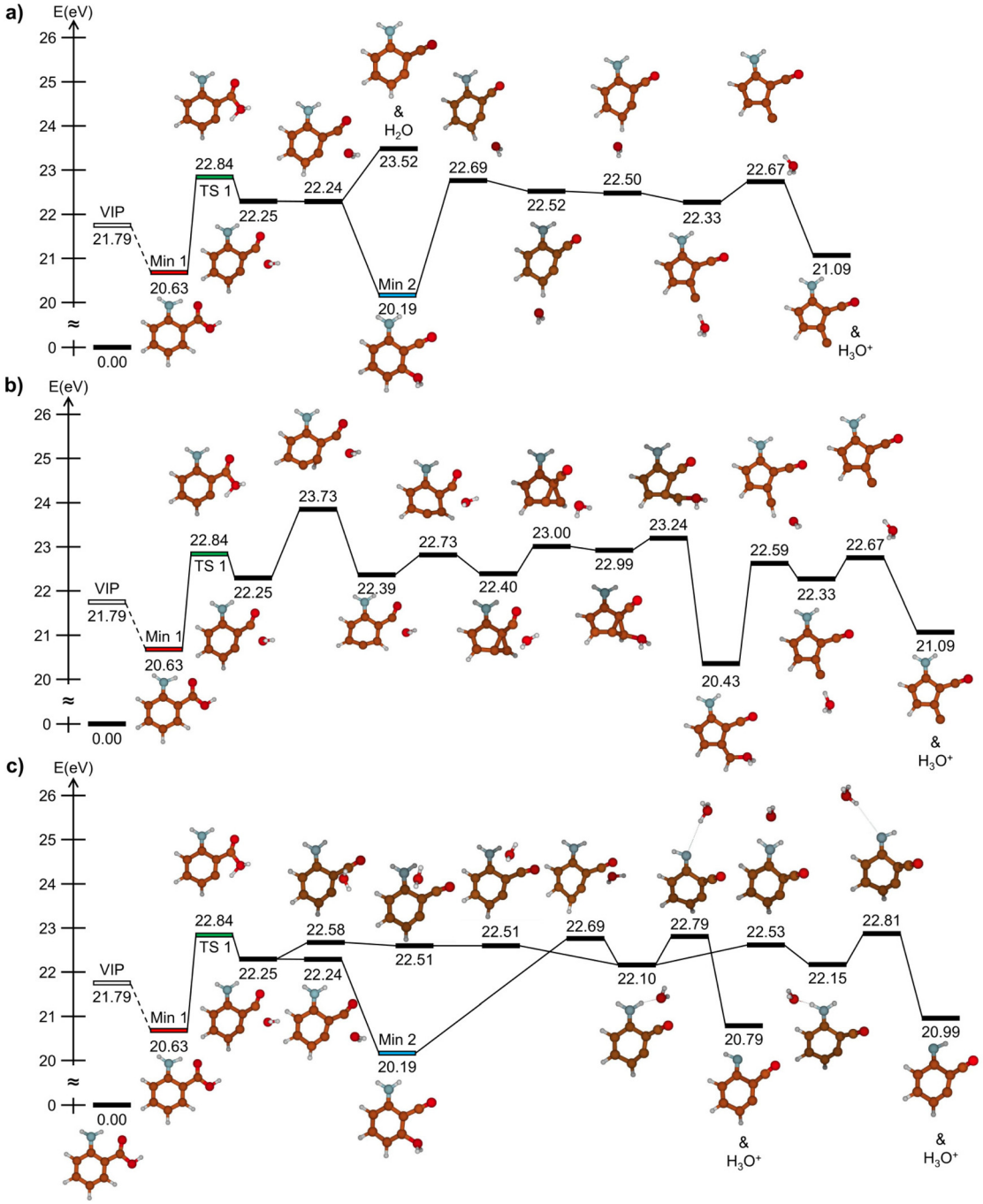

Fig. 4 Results of the potential energy surface (PES) exploration for dicationic *o*ABA with singlet spin multiplicity at the MP2/cc-pVDZ level. Energies include zero-point corrections and are referred to the neutral ground state. (a) A straightforward pathway to H_3O^+ emission through hydrogen migration and water roaming. The energy needed to release neutral water is also depicted. (b) A more complex series of hydrogen migrations to produce H_3O^+. (c) H_3O^+ is produced after the roaming water abstracts a proton from the NH_2 group instead of the benzene ring. Note that relevant points in the PES are highlighted with a coloured bar: Min 1 in red, Min 2 in blue and TS 1 in green.

greater stability is the intramolecular hydrogen bonding between the functional groups H–N–H···O–C–O–H.[56] Based on our calculations, the relaxation from the VIP to the dicationic minimum Min 1 further strengthens this bond. Specifically, the N–O and H–O distances in the hydrogen bond are shortened by 0.17 Å and 0.37 Å, respectively, creating a sort of double-ring structure for the dicationic *o*ABA1. To verify this, we have performed a bonding analysis in the Min 1 structure using the quantum theory of atoms in molecules, QTAIM,[57,58] as implemented in the AIMAll program.[59] The results of this analysis are presented in Fig. 5. Part of the positive charge is located in the amino group, which undergoes planarization. Electrons in one of the lone pair of the carboxylic oxygen are attracted with higher intensity towards the hydrogen atom in

Open Access Article. Published on 22 April 2025. Downloaded on 12/6/2025 4:39:31 PM.
This article is licensed under a Creative Commons Attribution 3.0 Unported Licence.

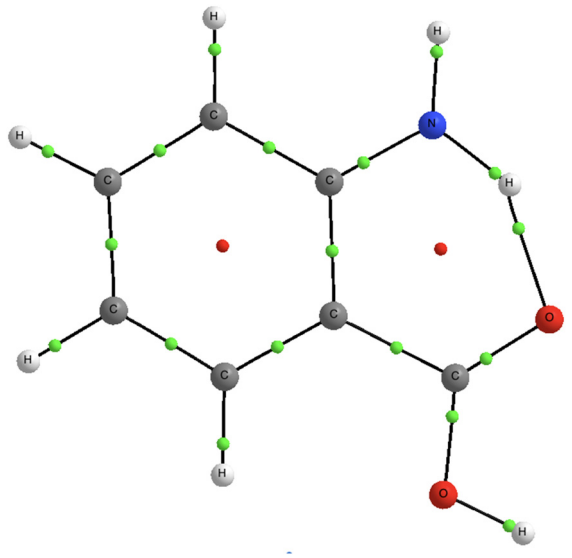

Fig. 5 QTAIM analysis of Min 1. Black lines are bond paths; green points are bond critical points and small red points are ring critical points.

the amino group, thus giving rise to a strengthening of the hydrogen bond with respect to the neutral molecule, creating a double-ring structure. A similar effect has been observed in the ionization of γ-aminobutyric acid.[6]

The key differences in fragmentation pathways between the ABA isomers can be seen in the TOF spectra in Fig. 2. The *m*ABA and *p*ABA spectra are missing the 59.5 *m*/*z* peak (*i.e.* $[M–H_2O]^{2+}$), but instead have notable peaks at 54.5 *m*/*z*, which can either be $[M–CNH_2]^{2+}$ or $[M–CO]^{2+}$, both of which imply a breakup of one of the functional groups. For *p*ABA specifically the 68.5 *m*/*z* peak (*i.e.* $[M]^{2+}$) is very weak, indicating that the dication is very unstable. We propose that the double ring structure that is formed in dicationic *o*ABA1 stabilises the functional groups, suppressing the competing fragmentation channels that are observed in the *meta*- and *para*-isomers, allowing for the migration and roaming processes that are necessary for H_3O^+ and H_2O production.

The fragmentation processes were also simulated using molecular dynamics simulations. A small sample of trajectories were computed with internal energies of 2 or 5 eV and propagation times of 500–1000 fs. However, with these energies and propagation times, the simulations produced no fragmentation. Therefore the bulk of simulations were run using internal energies of 10, 20 and 30 eV. These higher internal energies were needed in the simulations to produce fragmenting trajectories within short propagation times, but this is problematic because in the Auger electron–photoion coincidences, we observe the H_3O^+ channel already at 1.2 eV. A propagation time of 250 fs was chosen for the computational feasibility of a large number of trajectories. For the 10, 20 and 30 eV simulations ∼90%, ∼60% and ∼20% of trajectories remained unfragmented, respectively. The full results of the molecular dynamics simulations can be found in the ESI.† We can thus conclude that 250 fs may be enough time to describe dynamics at higher energies but is insufficient closer to the potential energy surface. The Auger electron–photoion coincidence measurements also show that this is exactly the energy range where H_3O^+ fragments are produced. In the experimental setup, the flight time of ionized particles is on the order of microseconds, so a molecule will have orders of magnitude more time to reach the available fragmentation pathways. Thus, the low energy dynamics are far better described by the MP2 PES exploration rather than the molecular dynamics simulations. Some H_2O and a handful of H_3O^+ producing trajectories were seen in the molecular dynamics, however without any notable isomer discrepancy. One such trajectory is depicted in Fig. 6, which closely resembles the pathway in Fig. 4(a), thus confirming the proposed mechanism.

Conclusions

In summary, we present a combined experimental and computational study of the fragmentation of *ortho*-aminobenzoic acid following C 1s photoionization and Auger decay. We present energy-resolved Auger electron–photoion coincidence (AEPICO) measurements which reveal that H_3O^+ ions are mostly (and their two-body dissociation counterparts, $[M–H_3O]^+$ ions, almost exclusively) detected in coincidence with high kinetic

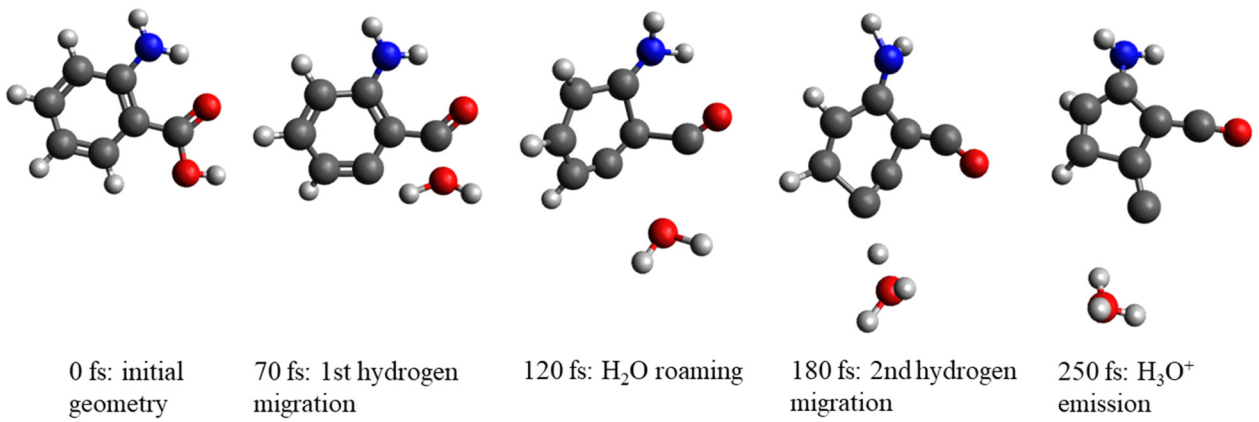

Fig. 6 Snapshots from a simulated 20 eV internal energy trajectory depicting H_3O^+ formation in *o*ABA. The trajectory is similar to the pathway in Fig. 4(a).

Open Access Article. Published on 22 April 2025. Downloaded on 12/6/2025 4:39:31 PM. This article is licensed under a Creative Commons Attribution 3.0 Unported Licence.

energy Auger electrons with a very narrow energy range around 268 eV. Thus, the fragmentation of *ortho*-aminobenzoic acid yielding H_3O^+ ions predominantly occurs within a specific range of internal energies. Modeling the dicationic excited states allows us to identify the electronic states contributing to the stable dication and H_3O^+ signals in the AEPICO measurements. Our potential energy surface exploration using quantum chemistry methods reveals multiple possible pathways for H_3O^+ production with activation energies that match the experimental H_3O^+ signal onset. We also propose an explanation for the isomer dependency in the H_3O^+ production based on the increased stability due to a double ring structure in the dicationic *o*ABA ground state, which suppresses the competing fragmentation mechanisms seen in the *meta*- and *para*-isomers.

Author contributions

O. V.: conceptualisation, formal analysis, funding acquisition, investigation, visualisation, writing – original draft. A. R. A.: conceptualisation, investigation, writing – review & editing. M. B., L. P., A. K., N. W.: investigation, writing – review & editing. E. K.: resources, software, investigation, writing – review & editing. M. H., S. U.: funding acquisition, writing – review & editing. M. A.: resources, supervision, writing – review & editing. O. B.: conceptualisation, writing – review & editing. M. P.: conceptualisation, formal analysis, funding acquisition, investigation, visualisation, writing – original draft. S. D.-T.: conceptualisation, formal analysis, funding acquisition, investigation, resources, visualisation, writing – original draft.

Data availability

Data for this article are available at the following URL/DOI: **https://doi.org/10.23729/42b5718f-10e0-41cb-89c2-0725a95068e9**.

Conflicts of interest

There are no conflicts to declare.

Acknowledgements

The authors acknowledge the CSC – IT Center for Science, Finland, for computational resources. The research leading to these results has been supported by the European Union's Horizon 2020 Research and Innovation Programme under the Marie Skłodowska-Curie I4Future (Grant agreement No. 713606). OV acknowledges the COST Action CA18222 (Attosecond Chemistry). This project was also granted travel funding from CALIPSOPlus from the EU Framework Programme for Research and Innovation Horizon 2020 (Grant agreement No. 730872). ARA acknowledges the Väisälä Fund and the Finnish Academy of Science & Letters. We acknowledge the Research Council of Finland for financial support (including The University of Oulu and Research Council of Finland Profi5 – project 326291 and INTRICat project 341288). We thank Drs K. Chernenko, E. Pelimanni and N. Boudjemia for assistance during the experiments. We acknowledge MAX IV Laboratory for time on Beamline FinEstBeAMS under Proposals 20190884 and 20230302. Research conducted at MAX IV, a Swedish national user facility, is supported by the Swedish Research Council under contract 2018-07152, the Swedish Governmental Agency for Innovation Systems under contract 2018-04969, and Formas under contract 2019-02496. We acknowledge the generous allocation of computer time at the Centro de Computación Científica at the Universidad Autónoma de Madrid (CCC-UAM). This work was partially supported by the MICINN – Spanish Ministry of Science and Innovation – Project PID2022-138470NB-I00 funded by MCIN/AEI/10.13039/501100011033, and the 'María de Maeztu' (CEX2023-001316-M) Program for Centers of Excellence in R&D.

Notes and references

1 A. P. Demchenko, *BBA Adv.*, 2023, **3**, 100085.
2 M. B. Soley, P. E. Videla, E. T. J. Nibbering and V. S. Batista, *J. Phys. Chem. Lett.*, 2022, **13**, 8254–8263.
3 K.-C. Tang, C.-L. Chen, H.-H. Chuang, J.-L. Chen, Y.-J. Chen, Y.-C. Lin, J.-Y. Shen, W.-P. Hu and P.-T. Chou, *J. Phys. Chem. Lett.*, 2011, **2**, 3063–3068.
4 A. R. Abid, O. Veteläinen, N. Boudjemia, E. Pelimanni, A. Kivimäki, M. Alatalo, M. Huttula, O. Björneholm and M. Patanen, *J. Phys. Chem. A*, 2023, **127**, 1395–1401.
5 N. Kling, S. Díaz-Tendero, R. Obaid, M. Disla, H. Xiong, M. Sundberg, S. Khosravi, M. Davino, P. Drach, A. M. Carroll, T. Osipov, F. Martín and N. Berrah, *Nat. Commun.*, 2019, **10**, 2813.
6 M. Capron, S. Díaz-Tendero, S. Maclot, A. Domaracka, E. Lattouf, A. Ławicki, R. Maisonny, J.-Y. Chesnel, A. Méry, J.-C. Poully, J. Rangama, L. Adoui, F. Martn, M. Alcam, P. Rousseau and B. A. Huber, *Chem. – Eur. J.*, 2012, **18**, 9321–9332.
7 C. L. Hawkins and M. J. Davies, *Biochim. Biophys. Acta, Bioenerg.*, 2001, **1504**, 196–219.
8 T. J. Wasowicz and B. Pranszke, *J. Phys. Chem. A*, 2016, **120**, 964–971.
9 K. Aplin and R. McPheat, *J. Atmos. Sol.-Terr. Phys.*, 2005, **67**, 775–783.
10 D. Catone, M. C. Castrovilli, F. Nicolanti, M. Satta and A. Cartoni, *Phys. Chem. Chem. Phys.*, 2023, **25**, 25619–25628.
11 F. Arnold, D. Krankowsky and K. Marien, *Nature*, 1977, **267**, 30–32.
12 R. Martinez, A. N. Agnihotri, P. Boduch, A. Domaracka, D. Fulvio, G. Muniz, M. E. Palumbo, H. Rothard and G. Strazzulla, *J. Phys. Chem. A*, 2019, **123**, 8001–8008.
13 T. E. Cravens, R. L. McNutt Jr., J. H. Waite Jr., I. P. Robertson, J. G. Luhmann, W. Kasprzak and W.-H. Ip, *Geophys. Res. Lett.*, 2009, **36**, L08106.
14 N. Indriolo, D. A. Neufeld, M. Gerin, P. Schilke, A. O. Benz, B. Winkel, K. M. Menten, E. T. Chambers, J. H. Black, S. Bruderer, E. Falgarone, B. Godard, J. R. Goicoechea, H. Gupta, D. C. Lis, V. Ossenkopf, C. M. Persson, P. Sonnentrucker, F. F. S. van der Tak, E. F. van Dishoeck, M. G. Wolfire and F. Wyrowski, *Astrophys. J.*, 2015, **800**, 40.

 This journal is © the Owner Societies 2025

Open Access Article. Published on 22 April 2025. Downloaded on 12/6/2025 4:39:31 PM.
This article is licensed under a Creative Commons Attribution 3.0 Unported Licence.

15 J. Tang and T. Oka, *J. Mol. Spectrosc.*, 1999, **196**, 120–130.
16 F. F. S. van der Tak, S. Aalto and R. Meijerink, *Astron. Astrophys.*, 2008, **477**, L5–L8.
17 D. P. Glavin, J. P. Dworkin, C. M. O. Alexander, J. C. Aponte, A. A. Baczynski, J. J. Barnes, H. A. Bechtel, E. L. Berger, A. S. Burton, P. Caselli, A. H. Chung, S. J. Clemett, G. D. Cody, G. Dominguez, J. E. Elsila, K. K. Farnsworth, D. I. Foustoukos, K. H. Freeman, Y. Furukawa, Z. Gainsforth, H. V. Graham, T. Grassi, B. M. Giuliano, V. E. Hamilton, P. Haenecour, P. R. Heck, A. E. Hofmann, C. H. House, Y. Huang, H. H. Kaplan, L. P. Keller, B. Kim, T. Koga, M. Liss, H. L. McLain, M. A. Marcus, M. Matney, T. J. McCoy, O. M. McIntosh, A. Mojarro, H. Naraoka, A. N. Nguyen, M. Nuevo, J. A. Nuth, Y. Oba, E. T. Parker, T. S. Peretyazhko, S. A. Sandford, E. Santos, P. Schmitt-Kopplin, F. Seguin, D. N. Simkus, A. Shahid, Y. Takano, K. L. Thomas-Keprta, H. Tripathi, G. Weiss, Y. Zheng, N. G. Lunning, K. Righter, H. C. Connolly and D. S. Lauretta, *Nat. Astron.*, 2025, **9**, 199–210.
18 C. Potiszil, T. Ota, M. Yamanaka, C. Sakaguchi, K. Kobayashi, R. Tanaka, T. Kunihiro, H. Kitagawa, M. Abe, A. Miyazaki, A. Nakato, S. Nakazawa, M. Nishimura, T. Okada, T. Saiki, S. Tanaka, F. Terui, Y. Tsuda, T. Usui, S.-I. Watanabe, T. Yada, K. Yogata, M. Yoshikawa and E. Nakamura, *Nat. Commun.*, 2023, **14**, 1482.
19 T. Koga and H. Naraoka, *Sci. Rep.*, 2017, **7**, 636.
20 A. Pernet, J. Pilmé, F. Pauzat, Y. Ellinger, F. Sirotti, M. Silly, P. Parent and C. Laffon, *Astron. Astrophys.*, 2013, **552**, A100.
21 J. Wang, A. A. Nikolayev, J. H. Marks, A. M. Turner, S. Chandra, N. F. Kleimeier, L. A. Young, A. M. Mebel and R. I. Kaiser, *J. Am. Chem. Soc.*, 2024, **146**, 28437–28447.
22 J. H. Marks, J. Wang, B.-J. Sun, M. McAnally, A. M. Turner, A. H.-H. Chang and R. I. Kaiser, *ACS Cent. Sci.*, 2023, **9**, 2241–2250.
23 T. Shirota, N. Mano, M. Tsuge and K. Hoshina, *Rapid Commun. Mass Spectrom.*, 2010, **24**, 679–686.
24 K. Hoshina and M. Tsuge, *Chem. Phys. Lett.*, 2010, **489**, 154–158.
25 Y. Tamenori, K. Okada, K. Tabayashi, A. Hiraya, T. Gejo and K. Honma, *Chem. Phys. Lett.*, 2006, **433**, 43–47.
26 C. Ma, J. Zhou, E. Wang, T. Yang, Z. Xu, S. Jia, A. Dorn and X. Ren, *Laser Part. Beams*, 2021, **2021**, e23.
27 P. Suwannakham, S. Chaiwongwattana and K. Sagarik, *RSC Adv.*, 2018, **8**, 36731–36744.
28 P. Intharathep, A. Tongraar and K. Sagarik, *J. Comput. Chem.*, 2006, **27**, 1723–1732.
29 T. M. Di Palma and A. Bende, *J. Mass Spectrom.*, 2014, **49**, 700–708.
30 Y. Tamenori, K. Okada, K. Tabayashi, A. Hiraya, T. Gejo and K. Honma, *J. Chem. Phys.*, 2011, **134**, 204302.
31 S. Maclot, D. G. Piekarski, A. Domaracka, A. Méry, V. Vizcaino, L. Adoui, F. Martín, M. Alcamí, B. A. Huber, P. Rousseau and S. Díaz-Tendero, *J. Phys. Chem. Lett.*, 2013, **4**, 3903–3909.
32 D. G. Piekarski, R. Delaunay, S. Maclot, L. Adoui, F. Martín, M. Alcamí, B. A. Huber, P. Rousseau, A. Domaracka and S. Díaz-Tendero, *Phys. Chem. Chem. Phys.*, 2015, **17**, 16767–16778.
33 S. Maclot, R. Delaunay, D. G. Piekarski, A. Domaracka, B. A. Huber, L. Adoui, F. Martín, M. Alcamí, L. Avaldi, P. Bolognesi, S. Díaz-Tendero and P. Rousseau, *Phys. Rev. Lett.*, 2016, **117**, 073201.
34 M.-A. Hervé du Penhoat, A. Souchaud, A. Rajpal, R. Vuilleumier, M.-P. Gaigeot, I. Tavernelli, K. Fujii, A. Yokoya, S. Díaz-Tendero and M.-F. Politis, *Phys. Chem. Chem. Phys.*, 2024, **26**, 15693–15704.
35 P. Rousseau, D. G. Piekarski, M. Capron, A. Domaracka, L. Adoui, F. Martn, M. Alcam, S. Díaz-Tendero and B. A. Huber, *Nat. Commun.*, 2020, **11**, 3818.
36 E. Kukk, L. Pihlava, K. Kooser, C. Stråhlman, S. Maclot and A. Kivimäki, *Phys. Chem. Chem. Phys.*, 2023, **25**, 5795–5807.
37 K. Kooser, A. Kivimäki, P. Turunen, R. Pärna, L. Reisberg, M. Kirm, M. Valden, M. Huttula and E. Kukk, *J. Synchrotron Radiat.*, 2020, **27**, 1080–1091.
38 R. Pärna, R. Sankari, E. Kukk, E. Nõmmiste, M. Valden, M. Lastusaari, K. Kooser, K. Kokko, M. Hirsimäki, S. Urpelainen, P. Turunen, A. Kivimäki, V. Pankratov, L. Reisberg, F. Hennies, H. Tarawneh, R. Nyholm and M. Huttula, *Nucl. Instrum. Methods Phys. Res., Sect. A*, 2017, **859**, 83–89.
39 K. Chernenko, A. Kivimäki, R. Pärna, W. Wang, R. Sankari, M. Leandersson, H. Tarawneh, V. Pankratov, M. Kook, E. Kukk, L. Reisberg, S. Urpelainen, T. Käämbre, F. Siewert, G. Gwalt, A. Sokolov, S. Lemke, S. Alimov, J. Knedel, O. Kutz, T. Seliger, M. Valden, M. Hirsimäki, M. Kirm and M. Huttula, *J. Synchrotron Radiat.*, 2021, **28**, 1620–1630.
40 C. Nicolas and C. Miron, *J. Electron Spectrosc. Relat. Phenom.*, 2012, **185**, 267–272.
41 A. Hiltunen, S. Aksela, G. Víkor, S. Ricz, Á. Kövér and B. Sulik, *Nucl. Instrum. Methods Phys. Res., Sect. B*, 1999, **154**, 267–271.
42 G. Prümper and K. Ueda, *Nucl. Instrum. Methods Phys. Res., Sect. A*, 2007, **574**, 350–362.
43 E. Kukk, G. Snell, J. D. Bozek, W.-T. Cheng and N. Berrah, *Phys. Rev. A:At., Mol., Opt. Phys.*, 2001, **63**, 062702.
44 E. Kukk, K. Ueda, U. Hergenhahn, X.-J. Liu, G. Prümper, H. Yoshida, Y. Tamenori, C. Makochekanwa, T. Tanaka, M. Kitajima and H. Tanaka, *Phys. Rev. Lett.*, 2005, **95**, 133001.
45 C. Møller and M. S. Plesset, *Phys. Rev.*, 1934, **46**, 618–622.
46 J. Dunning and H. Thom, *J. Chem. Phys.*, 1989, **90**, 1007–1023.
47 H. Koch and P. Jørgensen, *J. Chem. Phys.*, 1990, **93**, 3333–3344.
48 J. F. Stanton and R. J. Bartlett, *J. Chem. Phys.*, 1993, **98**, 7029–7039.
49 H. B. Schlegel, J. M. Millam, S. S. Iyengar, G. A. Voth, A. D. Daniels, G. E. Scuseria and M. J. Frisch, *J. Chem. Phys.*, 2001, **114**, 9758–9763.
50 S. S. Iyengar, H. B. Schlegel, J. M. Millam, G. A. Voth, G. E. Scuseria and M. J. Frisch, *J. Chem. Phys.*, 2001, **115**, 10291–10302.

Open Access Article. Published on 22 April 2025. Downloaded on 12/6/2025 4:39:31 PM.
This article is licensed under a Creative Commons Attribution 3.0 Unported Licence.

51 H. B. Schlegel, S. S. Iyengar, X. Li, J. M. Millam, G. A. Voth, G. E. Scuseria and M. J. Frisch, *J. Chem. Phys.*, 2002, **117**, 8694–8704.
52 C. Lee, W. Yang and R. G. Parr, *Phys. Rev. B:Condens. Matter Mater. Phys.*, 1988, **37**, 785–789.
53 A. D. Becke, *J. Chem. Phys.*, 1993, **98**, 5648–5652.
54 W. J. Hehre, R. Ditchfield and J. A. Pople, *J. Chem. Phys.*, 1972, **56**, 2257–2261.
55 M. J. Frisch, G. W. Trucks, H. B. Schlegel, G. E. Scuseria, M. A. Robb, J. R. Cheeseman, G. Scalmani, V. Barone, G. A. Petersson, H. Nakatsuji, X. Li, M. Caricato, A. V. Marenich, J. Bloino, B. G. Janesko, R. Gomperts, B. Mennucci, H. P. Hratchian, J. V. Ortiz, A. F. Izmaylov, J. L. Sonnenberg, D. Williams-Young, F. Ding, F. Lipparini, F. Egidi, J. Goings, B. Peng, A. Petrone, T. Henderson, D. Ranasinghe, V. G. Zakrzewski, J. Gao, N. Rega, G. Zheng, W. Liang, M. Hada, M. Ehara, K. Toyota, R. Fukuda, J. Hasegawa, M. Ishida, T. Nakajima, Y. Honda, O. Kitao, H. Nakai, T. Vreven, K. Throssell, J. A. Montgomery, Jr., J. E. Peralta, F. Ogliaro, M. J. Bearpark, J. J. Heyd, E. N. Brothers, K. N. Kudin, V. N. Staroverov, T. A. Keith, R. Kobayashi, J. Normand, K. Raghavachari, A. P. Rendell, J. C. Burant, S. S. Iyengar, J. Tomasi, M. Cossi, J. M. Millam, M. Klene, C. Adamo, R. Cammi, J. W. Ochterski, R. L. Martin, K. Morokuma, O. Farkas, J. B. Foresman and D. J. Fox, *Gaussian 16 Revision C.02*, Gaussian Inc., Wallingford, CT, 2016.
56 B. C. M. Maciel and P. Chaudhuri, *Int. J. Quantum Chem.*, 2011, **111**, 1709–1718.
57 R. F. W. Bader, *Chem. Rev.*, 1991, **91**, 893–928.
58 R. F. W. Bader, *Atoms in Molecules: A Quantum Theory*, Oxford University Press, Oxford, 1990.
59 T. A. Keith, *AIMAll (Version 19.10.12)*, TK Gristmill Software, Overland Park KS, USA, 2019 (**https://aim.tkgristmill.com**).

 This journal is © the Owner Societies 2025